Age, Genetics, and Crystallization Sequence of the Group IIIE Iron Meteorites

Emily M. Chiappe (echiappe@umd.edu), Richard D. Ash, and Richard J. Walker
Department of Geology, University of Maryland, College Park, Maryland, 20742, USA

Abstract

Chemical and isotopic data were obtained for ten iron meteorites classified as members of the IIIE group. Nine of the IIIE irons exhibit broadly similar bulk siderophile element characteristics. Modeling of highly siderophile element abundances suggests that they can be related to one another through simple crystal-liquid fractionation of a parent melt. Our preferred model suggests initial S, P, and C concentrations of approximately 12 wt.%, 0.8 wt.%, and 0.08 wt.%, respectively. The modeled IIIE parent melt composition is ~4 times more enriched in highly siderophile elements than a non-carbonaceous (NC) chondrite-like parent body, suggesting a core comprising ~22% of the mass of the parent body. Although chemically distinct from the other IIIE irons, formation of the anomalous IIIE iron Aletai can potentially be accounted for under the conditions of this model through the non-equilibrium mixing of an evolved liquid and early formed solid. Cosmic ray exposure-corrected nucleosynthetic Mo, Ru, and W isotopic compositions of four of the *bona fide* IIIE irons and Aletai indicate that they originated from the non-carbonaceous (NC) isotopic domain. Tungsten-182 isotopic data for the IIIE irons and Aletai yield similar model metal-silicate segregation ages of 1.6 ± 0.8 Myr and 1.2 ± 0.8 Myr, respectively, after calcium aluminum-rich inclusion (CAI) formation. These ages are consistent with those reported for other NC-type iron meteorite parent bodies. The IIIE irons are chemically and isotopically similar to the much larger IIIAB group. Despite some textural,

mineralogical, and chemical differences, such as higher C content, the new results suggest they may have originated from a different crystallization sequence on the same or closely-related parent body.

Keywords: IIIE iron meteorites, highly siderophile elements, fractional crystallization, Hf-W chronometry, meteorite genetics

1. Introduction

Magmatic iron meteorites are commonly interpreted to be fragments of asteroidal cores, with members of a group assumed to be related to one another through solid metal-liquid metal fractionation processes (e.g., Scott, 1972). The group IIIE meteorites are a magmatic iron group currently comprising seventeen members. Two members of the group, Aletai and Aliskerovo, are classified as "anomalous" based upon reportedly high Ir and Au concentrations relative to the other IIIE irons (*Meteoritical Bulletin*, 2022; Bouvier et al., 2017). The IIIE irons are characterized by moderate depletions in the volatile siderophile elements (e.g., Ga and Ge) and are structurally classified as coarse octahedrites (Scott and Wasson, 1973; Scott and Wasson, 1975). The IIIE irons exhibit similar Ga, Ge, and Ni concentrations as the much larger IIIAB group, but are distinguished by their coarser kamacite bandwidths, as well as by the presence of the C-rich minerals haxonite ($[Fe, Ni]_{23}C_6$) and graphite, which are absent in the IIIAB irons (Scott and Wasson, 1973).

Planetary materials have been characterized through the utilization of so-called "genetic" isotopes, which have revealed nucleosynthetic isotope heterogeneity between bulk planetary materials, suggesting the presence of at least two isotopically distinct nebular domains in the solar nebula (e.g., Trinquier et al., 2007; Trinquier et al., 2009;

Warren, 2011; Fisher-Gödde et al., 2015; Budde et al., 2016; Kruijer et al., 2017). This dichotomy likely reflects the heterogeneous distribution of nucleosynthetic components throughout the protoplanetary disk and, therefore, the heterogeneous accretion of material to parent bodies in each domain. This nucleosynthetic heterogeneity has been identified in meteorites across numerous elements, including Ti, Cr, Ni, Mo, W, and Ru, and has led to the recognition of the carbonaceous chondrite (CC) and non-carbonaceous (NC) meteorite classification scheme (Warren, 2011). It has been suggested that these two domains were initially isolated from one another by the formation of proto-Jupiter, which has led to the interpretation of NC- and CC-type meteorites sampling the inner and outer solar system, respectively (Warren, 2011; Budde et al., 2016; Kruijer et al., 2017). Other interpretations have also been proposed to explain the genetic dichotomy, such as the existence of a ringed protoplanetary disk or the migration of the water snow line (e.g., Brasser and Mojzsis, 2020; Lichtenberg et al., 2021).

The siderophile nature of Mo, Ru, and W makes these elements especially useful in the study of nucleosynthetic variability recorded in iron meteorites, with most magmatic iron meteorite groups having been classified as belonging to the NC- (IC, IIAB, IIIAB, IIIE, IVA) or CC-type (IIC, IID, IIF, IIIF, IVB) classification (e.g., Fischer-Gödde et al., 2015; Budde et al., 2016; Poole et al., 2017; Kruijer et al., 2017; Bermingham et al., 2018). Recent study of the Mo, W, and Ru compositions of the group IIIE irons has shown them to be NC-type meteorites (Kruijer et al., 2017; Worsham et al., 2019).

The ^{182}Hf-^{182}W system ($t_{1/2}$ = 8.9 Myr; Vockenhuber et al., 2004) is often applied to iron meteorites in the assessment of the thermal evolution, accretion age, and core formation age of their respective parent bodies (Kruijer et al., 2017; Hilton et al., 2019;

Tornabene et al., 2020). A range of ^{182}W isotopic compositions have been observed within and between NC and CC iron meteorites, reflecting different timescales of metal-silicate segregation and accretion, with NC-type iron meteorite groups, on average, yielding older core formation ages than CC-type iron meteorite groups (Kruijer et al., 2017; Spitzer et al., 2021). Hellmann et al. (2019), however, concluded that NC and CC iron meteorite parent body precursor materials may have evolved with variable Hf/W ratios, resulting in some ^{182}W model ages as much as ~0.7 Myr younger or older than previously thought.

The Mo, Ru, and W isotopic compositions of a meteorite can be modified by secondary neutron capture reactions triggered by cosmic ray exposure (CRE; Wittig et al., 2013; Kruijer et al, 2013). The degree to which an isotopic composition is modified is dependent on the duration and intensity of the cosmic ray flux, and the depth of a sample from the surface (Markowski et al., 2006). In order to obtain meaningful genetic data, these effects must be quantified and corrected for where necessary using a dosimeter, ideally analyzing the same meteorite piece used for genetic analysis. Here, Pt isotopic data are utilized as a dosimeter, as $^{196}Pt/^{195}Pt$ ratios are sensitive to secondary neutron capture reactions triggered by CRE, and become increasingly higher with CRE flux (Kruijer et al., 2013; Worsham et al., 2019).

The object of this study is to utilize HSE concentrations to assess the possible relationship between ten of the group IIIE iron meteorites through crystal-liquid fractionation modeling, to assess Mo, Ru, and W genetic characteristics, and to further constrain the thermal history and timing of metal-silicate segregation of the IIIE parent body core through the application of the ^{182}Hf-^{182}W system. Taken together, these data advance understanding of the structure and composition of the early solar system by

providing new insights into the chemical compositions, genetics, and ages of planetary bodies sampled by iron meteorites.

2. Samples

Seven group IIIE iron meteorite samples were obtained from the Smithsonian Institution National Museum of Natural History: Coopertown (USNM 1003), Kokstad (USNM 488), Paloduro (USNM 6877), Rhine Villa (USNM 272), Staunton (USNM 2204), Tanokami Mountain (USNM 1456), and Willow Creek (USNM 900). Burlington (ASU 978) and Colonia Obrera (ASU 1032) were obtained from Arizona State University. Aletai was obtained from KD Meteorites, Kansas.

3. Analytical Methods

3.1 Laser Ablation Inductively Coupled Plasma Mass Spectrometry (LA-ICP-MS)

We followed the procedures for the analysis of iron meteorites outlined in earlier publications (e.g., Walker et al, 2008; McCoy et al., 2011; Hilton et al., 2020; Tornabene et al., 2020). Each sample was cut into a 100-200 mg piece using a water-cooled *Leco Vari-cut* saw equipped with a diamond-impregnated sawblade. Cross-contamination between samples was avoided by cleaning the sawblade with water and replacing the cooling water after each cut. A piece of carborundum was also cut between each sample to further clean the blade. Samples were then polished with sandpapers of diminishing grit size to ensure that flat surfaces were removed of blade markings and rust. Immediately prior to analysis, samples were ultrasonicated in ethanol to remove any additional contaminants. Concentrations of 18 siderophile elements (Re, Os, W, Ir, Mo, Ru, Pt, Rh, Ni, Co, Fe, Pd,

Cr, P, As, Au, Ga, Ge) were obtained using a *New Wave UP213* ultraviolet laser coupled to a *Thermo Finnigan Element 2* inductively coupled mass spectrometer (ICP-MS). Ablation tracks were drawn to attempt to avoid the presence of sulfides, phosphides, and carbon phases. Data were processed using *LAMTRACE* (Rusk, 2009), using known concentrations of in-house laboratory reference iron meteorites Hoba, Coahuila, and Filomena. For each analysis, following blank subtraction, Fe+Ni+Co abundances were forced to sum to 100% (Campbell and Humayun, 2005). Multiple bulk ~5 mm long laser ablation tracks were averaged in order to obtain a representative composition of each sample.

3.2 ^{187}Re-^{187}Os and Highly Siderophile Element Analysis

Concentrations of Re, Os, Ir, Ru, Pt, and Pd, as well as ^{187}Re-^{187}Os data, were obtained by isotope dilution of bulk samples, following the procedures outlined in Walker et al. (2008). The highly siderophile elements Rh and Au were not included in this analysis due to their monoisotopic nature. Approximately 70-250 mg pieces of each sample were cut and polished. Each piece, along with appropriate amounts of a mixed spike containing ^{185}Re-^{190}Os and a separate mixed spike of ^{191}Ir-^{99}Ru-^{194}Pt-^{105}Pd was added to a *Pyrex*® Carius tube, along with 2.5 mL of concentrated HCl and 5 mL of concentrated HNO_3. Each tube was sealed and heated at ~220ºC for 24-48 hours to obtain complete dissolution and sample-spike equilibrium. This high-temperature digestion oxidizes Os to a +8 valence, forming osmium tetroxide (OsO_4). After dissolution, Os was separated via the carbon tetrachloride (CCl_4) solvent extraction technique outlined in Cohen and Waters (1996) and further purified by microdistillation as described in Birck et al. (1997). The purified Os

was loaded onto a Pt filament with a Ba hydroxide activator and analyzed using a *Thermo Fisher Triton* thermal ionization mass spectrometer (TIMS). Osmium isotopic data were corrected for instrumental mass fractionation by normalizing $^{190}Os/^{188}Os$ to 3.08271 (Allègre and Luck, 1980).

The residual acid containing the remaining HSE was evaporated to dryness, and the residue redissolved in 1M HCl. This was repeated once more to ensure removal of any remaining HNO_3. The samples were then loaded onto anion exchange columns in 1M HCl (Rehkämper and Halliday, 1997). Rhenium and Ru were eluted with 12 mL of 6M HNO_3, Pt and Ir were eluted with 13 mL of concentrated HNO_3, and Pd was eluted with 14 mL of concentrated HCl. The Re and Ru aliquots were further purified using a secondary anion exchange column and eluted with 7 mL of 6M HNO_3. Rhenium, Ru, Ir, Pt, and Pd isotope ratios were analyzed using a *Thermo Fisher Neptune Plus* multi-collector ICP-MS. Tungsten was added to the Re aliquots to correct for mass fractionation effects. Blanks for these procedures (n = 3) averaged 3, 4, 4, 43, 33, and 40 pg for Re, Os, Ir, Ru, Pt, and Pd, respectively. Blank corrections were made but had negligible impact on final concentration determinations. Estimated 2SD measurement uncertainties for Re and Os are < 0.1% and $\leq$ 2% for the other HSE.

3.3 Molybdenum, Ru, W, and Pt Isotopic Measurements

Isotopic analyses of Mo, Ru, W, and Pt were obtained through the digestion and chemical separation of the elements from approximately 2-5 g pieces of the samples. The amount of material required for digestion is dependent on the bulk Mo, Ru, W, and Pt concentration of each individual iron. Isotopic compositions for these elements are reported using the μ notation (e.g., Mo):

165 $$\mu^{94}\mathrm{Mo} = \left(\frac{^{94}_{96}\mathrm{Mo}_{\mathrm{sample}}}{^{94}_{96}\mathrm{Mo}_{\mathrm{standard}}} - 1\right) * 10^6$$

166

167 Each meteorite chunk was dissolved in 40mL of 8M HCl per 2g of sample at
168 ~140ºC for at least 48 hours in *Teflon*® beakers. The resulting solution was separated into
169 two aliquots to be processed separately. One aliquot was processed for Mo, W, and Pt using
170 a scaled-up version of the anion exchange column procedure described by Nagai and
171 Yokoyama (2014). Following this procedure, W was eluted with 100 mL of 9M HCl + 1M
172 HF, Mo with 50 mL of 6M HNO_3 + 3M HF, and Pt with 75 mL of concentrated HNO_3.
173 After the initial primary column, the resulting Mo aliquots were dried, redissolved
174 in 0.5 mL of 6M HCl, and loaded onto a secondary anion exchange column with ~0.3 mL
175 AG 1 x 8 200-400 mesh resin, following the chemical separation techniques outlined in
176 Worsham et al. (2016a). Molybdenum was then eluted with 12.5 mL of 1M HCl. This
177 secondary column elution scheme was repeated once to ensure sufficient purification. The
178 Mo aliquots were dried, re-dissolved in a 2:1 mixture of concentrated HNO_3 and HCl (100
179 µL), and dried again. This was repeated two more times to ensure removal of any resin-
180 derived organics. Samples were then re-dissolved in 6M HCl. Approximately 1000 ng of
181 Mo from each sample were loaded onto outgassed Re filaments along with 2 µL of a 5
182 µg/µL $La(NO_3)_3$ activator solution. Following the double filament assembly described in
183 Worsham et al. (2016a), a second filament was also prepared for each sample with 2 µL of
184 a 5 µg/µL $La(NO_3)_3$ activator. Molybdenum was analyzed as MoO^-_3 using a *Thermo Fisher*
185 *Triton Plus* TIMS using a 3-peak jump, multi-dynamic method. Isotopic data were
186 corrected for instrumental mass fractionation by normalizing $^{98}Mo/^{96}Mo$ to 1.453171 (Lu
187 and Masuda, 1994). Analytical uncertainties were assessed by repeatedly measuring

standards during the measurement campaign and determining their external reproducibility (2SD). Samples were analyzed during several short campaigns over an eight-month long period. The maximum 2SD of repeated analyses of the laboratory standard for any one campaign were ±42, ±14, ±10, ±6, and ±22 ppm for μ^{92}Mo, μ^{94}Mo, μ^{95}Mo, μ^{97}Mo, and μ^{100}Mo, respectively (n = 12).

Tungsten aliquots from the initial primary column were dried, re-dissolved in 0.6 mL of 0.4M HCl + 0.5M HF, and loaded onto a secondary column with ~0.2 mL AG 1 x 8 200-400 mesh resin, following procedures outlined in Nagai and Yokoyama (2014). Tungsten was eluted with 2.4 mL of 9M HCl + 3M HF. This column procedure was repeated once more to ensure W separation. The purified W aliquots were dried and redissolved in 0.4M HCl + 0.5 M HF. Approximately 1000 ng of W from each sample was loaded onto an outgassed Re filament along with 1 µL of 5 µg/µL La- 5 µg/µL Gd activator solution and measured as WO^-_3 using a *Thermo Fisher Triton* TIMS following measurement techniques outlined in Archer et al. (2017). Isotopic data were corrected for instrumental mass fractionation by normalizing $^{186}W/^{184}W$ to 0.92767 (Völkening et al., 1991). The 2SD external precision for this analytical campaign, as defined by repeated analyses of the standard, was ± 6 ppm for μ^{182}W and ± 3 ppm for μ^{183}W (n = 5) and is comparable to the precision reported by Kruijer et al. (2017) and Spitzer et al. (2021).

Platinum aliquots were dried, re-dissolved in a 2:1 mixture of concentrated HNO_3 and HCl, and refluxed overnight at 100ºC, following the clean-up procedure described in Hunt et al. (2017). Samples were then dried and refluxed overnight in 1M HCl, then diluted with ascorbic acid and loaded onto an anion exchange column with ~1 mL AG 1 x 8 200-400 mesh resin. Platinum was eluted with 15 mL of concentrated HNO_3. This column

procedure was repeated once more to ensure complete Pt-Ir separation. Solutions were dried, treated with $HClO_4$, and refluxed overnight in 2:1 HNO_3 and HCl. Samples were dried once more and taken up in 5% HNO_3 to be analyzed on a *Thermo Fisher Neptune Plus* multi-collector ICP-MS. Isotopic data were corrected for instrumental mass fractionation by normalizing $^{198}Pt/^{195}Pt$ to 0.21450 (Kruijer et al., 2013). The 2SD external precision for this analytical campaign, as defined by repeated analyses of the standard, was ± 8 ppm for $\mu^{196}Pt$ (n = 20).

The second aliquot from the initial 8M HCl digestion was processed for Ru following methods outlined in Bermingham et al. (2016). Ruthenium aliquots were dried, redissolved in 0.15M HCl, and loaded onto a primary cation column with 10 mL AG50W8X 200-400 mesh resin, and eluted with 15 mL of 0.15M HCl. Ruthenium was further purified via microdistillation using 0.2 g/mL CrO_3 in 0.5M H_2SO_4 and 4M HBr. After microdistillation, samples were taken up in 5% HNO_3 and analyzed using a *Thermo Fisher Neptune Plus* multi-collector ICP-MS following measurement techniques similar to those outlined in Fischer-Gödde et al. (2015). Isotopic data were corrected for instrumental mass fractionation by normalizing $^{99}Ru/^{101}Ru$ to 0.745075 (Chen et al., 2010). The 2SD external precision for this analytical campaign, as defined by repeated analyses of the standard, was ± 8 ppm for $\mu^{100}Ru$ (n = 15).

4. Results

4.1 Bulk composition analysis by LA-ICP-MS

Bulk compositional data for the IIIE iron meteorites determined via LA-ICP-MS along with their two-standard deviation (2SD) variation for each element for the combined tracks are given in **Table 1**. Rhenium concentrations were below detection limits for all

samples except Kokstad, Colonia Obrera, and Aletai. Substantial heterogeneities in signal intensities along some measured tracks were observed for several elements (e.g., Cr and P) due to the intersection of the ablation tracks with non-metal phases, such as sulfides and phosphides. Furthermore, kamacite-taenite partitioning led to variations in Ni and other elements. Bulk Ni concentrations obtained here, however, are largely within 15% of instrumental neutron activation analysis data reported by Scott et al. (1973) and Sugiura et al. (2000), with the exception of our small (< 2g), weathered sample of Tanokami Mountain, in which the preferential analysis of taenite led to high Ni (and some other elements) contents compared to literature values. Gallium and Ge concentrations are within 10%, and Ir concentrations are within 20% of reported concentrations. A comparison of the data reported here to those previously reported by Scott et al. (1973), Malvin et al. (1984), and Sugiura et al. (2000) is provided in **Table S1**.

The CI chondrite normalized bulk siderophile element data reveal broadly similar patterns for nine of the ten IIIE irons (**Fig. 1**). The data show moderate depletions in the volatile siderophile elements (e.g., Ga and Ge) relative to more refractory siderophile elements (e.g., Mo and W), consistent with their group III classification. There is also a significant depletion in Cr, likely a result of the element preferentially partitioning into daubréelite ($FeCr_2S_4$) rather than remaining in the metal phase. Additional depletions observed in some HSE, as discussed further below, are observed across all samples and are indications of the relatively evolved nature of the irons. The siderophile element abundance pattern for Aletai, however, deviates significantly from the patterns established by the other IIIE irons. This is noticeable, for example, in the higher Au and As contents, and lower Ru and Pt contents exhibited by the iron. Thus, as discussed further below, the composition of

Aletai is inconsistent with it forming as an equilibrium solid or via equilibrium mixing from the same crystal-liquid fractionation sequence from which the *bona fide* IIIE irons originate.

4.2 Highly siderophile element concentrations and Re-Os systematics

Highly siderophile element concentrations obtained by isotope dilution are reported in **Table 2**. CI chondrite-normalized data for bulk samples define nested HSE patterns that, for the most part, do not cross one another (**Fig. 2**). All of the irons analyzed here exhibit depletions in the strongly compatible elements Re, Os, and Ir, relative to Ru, Pt, and Pd. While the anomalous IIIE iron Aletai has Ni, Ga, and Ge concentrations similar to those of the other group IIIE irons, consistent with its original classification, the HSE abundances reported here differ substantially from the other IIIE irons. Aletai exhibits similar depletions in Re and Ir, but stronger depletions in Ru and Pt, relative to the other irons. The Os abundance of Aletai is also slightly enriched relative to most of the other IIIE irons and is inconsistent with the established trend.

Rhenium-Os isotopic data for the IIIE irons are provided in **Table 2** and are plotted relative to a 4.56 Ga reference isochron in **Figure 3**. The IIIE irons are characterized by a moderate range of $^{187}Re/^{188}Os$ and $^{187}Os/^{188}Os$ of 0.7542 to 1.0278 and 0.15678 to 0.17662, respectively. Willow Creek, Paloduro, Tanokami Mountain, and Aletai do not plot within uncertainties of the reference isochron, suggesting minor open-system behavior within those meteorites, possibly related to the inferred impacts to the parent body, or to terrestrial weathering processes. Weathering is particularly prevalent in Willow Creek and Tanokami Mountain (Buchwald, 1975). The remaining IIIE irons plot within uncertainty of the reference isochron, indicating closed-system behavior of siderophile elements in those

meteorites since early formation. Regression of the ^{187}Re-^{187}Os data for all samples apart from Aletai using ISOPLOT (Ludwig, 2003) yields an imprecise age of 4387 ± 440 Myr (2SD) and an initial $^{187}Os/^{188}Os$ of 0.0988 ± 0.0069 (2SD).

4.3 Platinum isotopic compositions and CRE correction

The $\mu^{196}Pt$ values for select IIIE irons and Aletai range from 3 ± 8 to 27 ± 8 (**Table 3**). Those that fall within the 2SD reproducibility of the $^{196}Pt/^{195}Pt$ ratio of the laboratory standard (± 8 ppm) are assumed to have been minimally affected by CRE, whereas those that fall outside of this range (Burlington, Kokstad, Tanokami Mountain, Aletai) are interpreted to have isotopic compositions modified by CRE. As all irons analyzed here, apart from Coopertown, fall outside of the range established by the standard, corrections for the Mo, Ru, and W isotopic compositions of these meteorites are necessary and reported and group corrections are reported in **Tables 4 - 5**. It should be noted that Spitzer et al. (2021) reported small nucleosynthetic Pt isotope anomalies observed in ungrouped CC iron meteorites and proposed that a starting $\mu^{196}Pt$ composition of -6, instead of 0 be used in CRE corrections of CC-type iron meteorites, and potentially extended to NC-type irons. As the proposed offset for NC-type meteorites has not yet been firmly established, corrections to a value of 0 are reported here. If an offset is confirmed for NC-type irons, then the model ages of all NC-type irons would be changed to ~ 1 Myr younger. Corrections of Mo and Ru isotopic data would result in negligible changes.

4.4 Molybdenum, Ru, and W isotopic compositions

Molybdenum, Ru, and W isotopic compositions for select IIIE irons and Aletai are reported in **Tables 4 and 5**. Aletai is treated as separate from the other IIIE irons due to its

differences in bulk siderophile element chemistry. The Mo data obtained here are consistent with previously reported Mo isotopic data for group IIIE irons (**Table S2**). The IIIE irons are characterized by CRE-uncorrected μ^{94}Mo values ranging from 80 ± 13 (2SD) to 100 ± 14, μ^{95}Mo values ranging from 27 ± 10 to 51 ± 8, and μ^{97}Mo values ranging from 19 ± 5 to 25 ± 4. Cosmic ray exposure-corrected group averages are 124 ± 40, 104 ± 14, 52 ± 10, 19 ± 5, and 18 ± 20 for μ^{92}Mo, μ^{94}Mo, μ^{95}Mo, μ^{97}Mo, and μ^{100}Mo respectively. Molybdenum data for Aletai were corrected using μ^{i}Mo-μ^{196}Pt slopes obtained by Spitzer et al. (2020) for the IIAB iron meteorites, as they are better constrained than the μ^{i}Mo-μ^{196}Pt slopes obtained for this study (**Table S3**). Slopes that were not reported directly in Spitzer et al. (2020) were calculated from their published data via a Model 1 regression using ISOPLOT (Ludwig, 2003). Several iron meteorite groups have been measured with respect to μ^{i}Mo-μ^{196}Pt variations, and μ^{i}Mo-μ^{196}Pt slopes are consistent across all groups, thus allowing for the correction of Aletai's isotopic compositions using the better-defined slopes. Cosmic ray exposure-corrected μ^{94}Mo, μ^{95}Mo, and μ^{97}Mo values for Aletai are 121 ± 14, 58 ± 8, and 22 ± 5, respectively.

The average CRE-corrected μ^{100}Ru value obtained for the IIIE irons is -47 ± 9, which is consistent with the group average of -51 ± 9 reported by Worsham et al. (2019). The CRE-corrected μ^{100}Ru value obtained for Aletai is -55 ± 8. The average μ^{183}W value obtained for the IIIE irons is 0 ± 3, which overlaps within uncertainty of the group average value of -5 ± 4 reported by Kruijer et al. (2017). The μ^{183}W value obtained for Aletai is -1 ± 3. The CRE-corrected Mo, Ru, and W isotopic data for Aletai are not resolved from the group IIIE averages.

5. Discussion

5.1 Fractional crystallization model

The variations seen in HSE concentrations among the IIIE iron meteorites, with the exception of Aletai, are broadly consistent with fractional crystallization from a common parent melt. With solid metal-liquid metal partition coefficients (D values) greater than 1, Re, Os, Ir, Ru, and Pt concentrations are expected to decrease in evolving solid and liquid metal as crystallization proceeds. Palladium, with a D value of less than 1 in melts with low S content (< 15 wt.%), normally increases through a crystallization sequence (Chabot et al., 2017). Similar to previous studies that explored crystallization processes of iron meteorite groups (e.g., McCoy et al., 2011; Hilton et al., 2020; Zhang et al., 2022), the origin of the IIIE irons by fractional crystallization can be further examined through detailed modeling of HSE behavior. To do so, appropriate D values for each element were calculated using parameterization methods developed by Jones and Malvin (1990) and advanced by Worsham et al. (2016b), Chabot et al. (2017), and Chabot and Zhang (2022). A detailed description of this approach is provided in the supplemental materials.

Concentrations of S, P, and C can greatly affect the partitioning behavior of siderophile elements during the crystallization of metallic liquids and therefore must be constrained in order to produce a successful crystallization model. An initial S content was estimated by following a similar method to that of Chabot et al. (2004) and Zhang et al. (2022), in which fractionation trends of Ga, Ge, and Ir were modeled under different starting S concentrations to achieve a best fit to the data. Gallium, Ge, Ir, and As were chosen due to the distinct non-linear trends they produce through a crystallization sequence that are particularly sensitive to starting S concentration (Wasson, 1999; Wasson and Richardson, 2001; Chabot et al., 2004). Best fits to Ga, Ge, Ir, and As trends suggest an initial S

concentration of 9 to 14 wt.% (**Fig. S2**). There is considerable scatter across the group, and Tanokami Mountain in particular noticeably deviates from the Ga-As, Ge-As, and Ir-As trends established by the rest of the IIIE irons, possibly as a consequence of terrestrial weathering processes experienced by the iron. All trends are otherwise best fit using the 12 wt.% S model. It is worth noting, however, that the relatively evolved nature of the IIIE irons makes estimating initial light element concentrations this way somewhat problematic, as concentrations are expected to increase in a melt as crystallization proceeds. The irons included here, therefore, likely reflect higher concentrations of light elements than their less evolved counterparts.

The effect of P on the model was estimated through the incorporation of the P vs. As trend of the group, following a similar method to that of Zhang et al. (2022), which provides an initial P concentration of 0.8 wt.% (**Fig. S3**). An initial C content was estimated by dividing the C concentration of the least evolved IIIE analyzed here, Coopertown, by a D_o of 0.37 (Worsham et al., 2016b). Using a C concentration of 285 ppm from Moore et al. (1969), this provides an initial C concentration of 0.08 wt.%. It is worth noting, however, that the analyses conducted by Moore et al. (1969) were targeted primarily on the metallic phase of the meteorites, thereby excluding larger carbide inclusions present in the samples, and consequently underestimating their overall C content. An initial C concentration of 0.08 wt.% is, therefore, likely a slight underestimation. In practice, due to their lower abundances relative to S, starting concentrations of P and C have less of an influence on HSE partitioning behavior. Thus, the most favorable light-element concentrations determined for this model are 12 wt.% S, 0.8wt.% P, and 0.08 wt.% C.

375 Highly siderophile element concentrations of the parent melt were then treated as free
376 parameters and varied until a model crystallization sequence was produced that matched
377 the observed HSE abundances of the IIIE irons, while also ensuring that modeled HSE
378 ratios of the initial liquid remained within the range established by chondrites. The
379 preferred model presented here is not a unique solution, as there are countless parent melt
380 compositions that can be modeled to produce a distinct iron meteorite composition. The
381 goal of the modeling conducted is to maximize the number of IIIE irons that can be
382 generated via a common fractional crystallization process. Modeled solid and liquid
383 evolution tracks for Re (ppb) versus Re/Os ratio are shown in **Figure 4** along with data for
384 the IIIE irons and Aletai. The initial parent melt HSE concentrations for this model are
385 provided in **Table 6**. The crystallization of all nine *bona fide* IIIE irons can be accounted
386 for under the conditions of this model. Coopertown, Burlington, and Kokstad plot directly
387 on the modeled solid track, defining equilibrium solids at ~30% fractional crystallization.
388 The remaining IIIE irons plot either directly on the liquid track or between the solid and
389 liquid tracks, indicating that these irons could have formed via fractional crystallization
390 with mixing of various amounts of trapped material. Aletai plots outside the bounds of this
391 model, but its formation can potentially be accounted for through the non-equilibrium
392 mixing of an evolved liquid and an early-formed solid (**Fig. 4**).
393 The incorporation of other HSE systematics under the same starting conditions can
394 account for the formation of all ten IIIE irons, with all irons except for Aletai plotting near
395 or directly on the solid track. (**Fig. 4**). This is in contrast to the solid metal-liquid metal
396 mixing required to justify the observed Re (ppb) versus Re/Os systematics of many of the
397 IIIE irons. This inconsistency can be explained by post-crystallization loss or gain of Re

and/or Os in some samples, or by minor discrepancies in the D values applied in the modeling. These observations are consistent, however, with the more limited variation in measured concentrations seen in elements like Pt and Ru when compared to Re and Os. This is also observed in the evolution of the modeled HSE patterns under these parental melt conditions (**Fig. 5**). Consistent with their crystallization as equilibrium solids, Coopertown, Burlington, and Kokstad follow the modeled HSE pattern at 30% fractional crystallization with minimal deviation. The other IIIE irons deviate from the modeled patterns, most noticeably in their Re, Os, and Ir concentrations, indicating that processes in addition to simple fractional crystallization were involved in their formation. Discrepancies between the modeled and measured HSE concentrations could also be a result of equilibrium and non-equilibrium solid-metal liquid-metal mixing, with influence from a more S-rich trapped melt.

The initial melt concentrations for HSE calculated for this model are shown in **Figure 6** compared to estimated HSE concentrations for other magmatic iron meteorite groups. The estimated HSE concentrations of the IIIE parent body core are ~4 times higher than that of a NC chondrite-like parent body, consistent with modeled parent melt compositions of other NC-type iron meteorite parent bodies. In contrast, more variable parent melt compositions are observed for CC-type iron meteorite parent bodies. This is most likely a reflection of the relative size of the core, and therefore the oxidation state, of the parent bodies. The CC-type bodies have been suggested to have formed under more oxidizing conditions than NC-type bodies (Hilton et al., 2022). Assuming that all HSE are sequestered into the core upon metal-silicate segregation, size of the IIIE core was ~22% by mass of the parent body. Normalizing the parent melt composition to Ni and CI

chondrite reveals a chondritic pattern consistent with that of other NC-type parent bodies, corresponding with their formation in a relatively reduced environment (**Fig. S4**; Zhang et al., 2022).

5.2 Genetics

The incorporation of varying amounts of *r-, s-,* and *p*-process nuclides between the NC and CC reservoirs of the early solar system have allowed for the "genetic" comparison of extraterrestrial materials. For example, CC-type meteorites have been shown to exhibit *s*-process depletions and *r*-process enrichments relative to NC-type meteorites (Budde et al, 2019; Spitzer et al., 2020). These signatures define two distinct mixing lines, as commonly illustrated on plots of μ^{94}Mo vs. μ^{95}Mo values of various extraterrestrial materials. Additionally, variations in $\mu^{92,94,97}$Mo relative to μ^{100}Ru have revealed a linear relationship among NC-type meteorites that is not observed in CC-type materials (Dauphas et al., 2004; Fischer-Gödde et al., 2015; Worsham et al., 2019). Instead, a correlation is seen in the μ^{183}W value of CC-type meteorites relative to their Mo isotopic compositions (Worsham et al., 2019). This correlation is absent in NC-type meteorites.

The IIIE irons have been previously reported to be NC-type (Kruijer et al., 2017; Worsham et al., 2019). The CRE-corrected Mo data obtained here are in agreement with this (**Fig. 7**). There are no resolved differences in the CRE-corrected Mo isotopic compositions of the *bona fide* IIIE irons analyzed here and Aletai, providing permissive evidence that they were all derived from the same parent body. The CRE-corrected Ru and μ^{183}W isotopic data reported here are also consistent with their NC classification (**Fig. 8-9**).

444

445 *5.3 Hf-W chronology*

446 The similar Mo, Ru, and W isotopic compositions of the IIIE irons and their relation
447 through a shared fractional crystallization process provide evidence for their origin from a
448 common parent body core. The W isotopic composition of the IIIE irons can therefore
449 provide temporal constraints on metal-silicate segregation of the IIIE parent body. Metal-
450 silicate segregation ages are commonly calculated relative to an initial solar system $\mu^{182}W$
451 value from CAI of -349 ± 7 (Kruijer et al., 2014) and a present-day chondritic $\mu^{182}W$ value,
452 based on measurements of carbonaceous chondrites, of -191 ± 8 (Kleine et al., 2004). The
453 average CRE-corrected $\mu^{182}W$ composition of the group IIIE irons is -331 ± 10 (**Fig. S1**)
454 and, using these parameters, yields a model core formation age of 1.6 ± 0.9 Myr after CAI
455 formation (**Fig. 9**). Both the average $\mu^{182}W$ composition and metal-silicate segregation age
456 reported here are consistent with those reported for the group IIIE iron meteorites by
457 Kruijer et al. (2017). The $\mu^{182}W$ value obtained for Aletai corresponds to a model core
458 formation age that overlaps with that of the IIIE irons, at 1.2 ± 0.9 Myr after CAI. Utilizing
459 the starting $\mu^{196}Pt$ composition of -6 proposed by Spitzer et al. (2021) for the CRE
460 corrections yields a model core formation age of 2.8 ± 1.0 Myr after CAI for the IIIE irons.
461 This is consistent with the revised age of 2.6 ± 0.8 Myr after CAI reported by Spitzer et al.
462 (2021).

463 It has been shown that ordinary chondrite precursors exhibit Hf/W ratios that are
464 significantly lower than those of carbonaceous chondrites, suggesting that using a
465 carbonaceous chondrite-like $\mu^{182}W$ value in model age calculations for NC-type material
466 may yield ages unrepresentative of material originating from the NC reservoir (Hellmann
467 et al., 2019). For example, the $^{180}Hf/^{184}W$ ratio reported by Hellmann et al. (2019) of ~0.7

for the ordinary chondrite precursor reservoir yields a metal-silicate segregation age of ~3 Myr after CAI formation for the IIIE parent body. Applying the same ordinary chondrite-like value to other NC iron parent bodies would result in a similar shift in previously reported model ages that were obtained using a carbonaceous chondrite-like $\mu^{182}W$ value.

5.4 Comparison to Group IIIAB

The chemical similarities between the IIIE and IIIAB irons were first noted by Scott and Wasson (1973). The IIIE irons exhibit similar Ga, Ge, Ir, and Ni abundances (**Fig. S5**) as the IIIAB irons but were designated as a separate group due to their wider kamacite bandwidths, as well as by the presence of C-rich minerals that have not been observed in the IIIAB irons. The two groups were marginally resolved from one another by Malvin et al. (1984) based on Co-, Cu-, As-, Au-, and W-Ni trends. Sugiura et al. (2000) also noted complete resolution of the two groups in terms of their Co-Au trends, however, this distinction is not observed in the data reported here (**Fig. S6**). The groups are not resolved from one another in terms of N isotopic compositions, but may exhibit slight differences in their C isotopic compositions (Sugiura et al., 2000). The Mo, Ru, and W isotopic compositions of the two groups are within uncertainty of one another, as well as with Aletai (Kruijer et al., 2017; Worsham et al., 2017; Bermingham et al., 2018; **Fig. S7-S9; Table S5**). The Mo and W isotope compositions of the IIIE irons are also similar to those of the main group pallasites, which have been proposed to be genetically linked to the IIIAB iron meteorite group (e.g., Kruijer et al., 2022). The IIIE and IIIAB irons also reveal broadly similar HSE abundances, with the IIIE irons exhibiting HSE patterns similar to those of the moderately fractionated IIIAB irons (**Fig. 10**). When included in the fractional crystallization model discussed here, all IIIAB irons for which data were available fall

within the bounds established by the model, except in the case of Re/Os vs. Re, wherein formation of the more fractionated irons is not accounted for (**Fig. S10**). Previous modeling of the IIIAB irons by Hilton et al. (2022) included five IIIAB irons with HSE abundances that were minimally affected by fractionation processes. These irons (Costilla Peak, Henbury, Charcas, Tamarugal, and Maldyak) are the five IIIAB irons that are accounted for with regard to their Re/Os vs. Re (ppb) systematics in the model discussed here. Further, the model discussed for the IIIAB irons in Hilton et al. (2022) includes parent melt parameters similar to those of the IIIE model proposed in this study, with the exception of C, which likely did not contribute as much to the formation of the IIIAB irons as it did with the IIIE irons, as evinced by the mineralogy of the two groups.

Despite differences in texture and mineralogy, the bulk HSE characteristics, genetics, and ages presented here of the IIIE and IIIAB irons are permissive of them sampling the same parent body. The two groups may be products of separate crystallization sequences, with the crystallization sequence that produced the IIIE irons richer in C than the crystallization sequence that produced the IIIAB irons. In the case of the two groups forming on separate parent bodies, they must have formed in the same nebular domain and experienced similar evolutionary processes in order to have produced the remarkably similar geochemical and isotopic compositions observed here.

5.5 Aletai

The Ga, Ge, Ir, and Ni concentrations exhibited by Aletai are similar to those of the IIIE irons, explaining its original classification as an anomalous IIIE iron. Additionally, Aletai's mineralogical and textural characteristics are similar to those of the group IIIE irons, further indicating a common origin (Breen et al., 2016). The HSE concentrations

exhibited by Aletai, however, do not fit the crystallization trend established by the other IIIE irons analyzed here and instead suggest either formation via non-equilibrium mixing of an evolved liquid and an early crystallized solid, or formation from a crystallization sequence distinct from that of the other IIIE irons. In the latter case, the similarities in genetics, age, and mineralogy between Aletai and the IIIE irons are still permissive of a common parent body origin, with Aletai possibly forming via the crystallization of a melt pocket on the IIIE parent body with a different starting composition and/or different D-values than the composition that produced the IIIE irons, resulting in the different HSE concentrations observed for Aletai. As with the IIIAB irons, in the case of Aletai sampling a separate parent body altogether, its formation would likely have occurred in the same nebular domain as the IIIE irons in order to produce isotopic compositions so similar to the group.

6. Conclusions

Nine of the IIIE irons analyzed here exhibit broadly similar bulk siderophile element characteristics. The siderophile element abundances of the anomalous IIIE iron Aletai, however, differ from those of the rest of the group. The nine *bona fide* IIIE irons can be related to one another through a common fractional crystallization process, assuming a parent melt containing 12 wt.% S, 0.8 wt.% P, and 0.08 wt.% C. Under the conditions of this model, formation of the anomalous IIIE iron Aletai requires non-equilibrium mixing of an evolved liquid and early formed solid to match observed HSE concentrations. Nucleosynthetic Mo, Ru, and W isotopic compositions indicate that the IIIE irons and Aletai are NC-type meteorites and sample the same nebular domain within the inner solar system. The Hf-W isotopic system indicates that the IIIE parent body underwent metal-

silicate segregation 1.6 ± 0.9 Myr after CAI, assuming a carbonaceous chondrite-like $\mu^{182}W$ value. The $\mu^{182}W$ composition for Aletai yields a similar core formation age of 1.2 ± 0.9 Myr after CAI. These ages are similar to those of other NC-type and CC-type iron meteorite parent bodies. All genetic and chronologic data reported here for Aletai overlap with those of the IIIE irons, providing further evidence that, despite its anomalous chemical characteristics, it likely sampled the same parent body core. Additionally, the chemical, genetic, and chronological characteristics shared among the IIIE and IIIAB irons are permissive of them sampling the same parent body. Their differences in chemistry, texture, and mineralogy may be explained through their formation via different crystallization sequences.

Acknowledgments

We gratefully acknowledge the Division of Meteorites, Department of Mineral Sciences, Smithsonian Institution, and the Arizona State University meteorite collection for providing the samples for this study. This study was supported by NASA Emerging Worlds grant 80NSSC20K0335 (to RJW).

Appendix A. Supplementary material

The supplementary materials for this article include a detailed description of the fractional crystallization modeling approach, as well as five tables (**Tables S1-S5**) and ten figures (**Figs. S1-S10**). **Tables S1-S3** and **S5** provide comparisons of previously published chemical and isotopic data for the IIIE iron meteorites with the data reported in this study. **Table S4** reports previously unpublished HSE data for the IIIAB irons. **Figure S1**

illustrates the CRE corrections made for the $\mu^{95}Mo$ and $\mu^{182}W$ isotopic compositions reported for the IIIE irons. **Figures S2** and **S3** include plots used to constrain initial S and P concentrations of the IIIE parent melt, and **Figure S4** shows the IIIE parent melt normalized to Ni and CI chondrite. **Figures S5-S10** include comparisons of chemical and isotopic data for the IIIE and IIIAB irons.

References

Allègre, C. J. and Luck, J. M. (1980) Osmium isotopes as petrogenetic and geological tracers. *Earth Planet. Sci. Lett.* **48**(1), 148–154.

Archer, G.J., Mundl, A., Walker, R.J., Worsham, E.A. (2017) High-precision analysis of 182W/184W and 183W/184W by negative thermal ionization mass spectrometry: Per-integration oxide corrections using measured 18O/16O. *Int. J. Mass Spectrom.* **414**, 80-86.

Bermingham, K. R., Walker, R. J., and Worsham, E. A. (2016) Refinement of high precision Ru isotope analysis using negative thermal ionization mass spectrometry. *Int. J. Mass Spectrom.* **403**, 15-26.

Bermingham, K. R., Worsham, E. A., and Walker, R. J. (2018) New insights into Mo and Ru isotope variation in the nebula and terrestrial planet accretionary genetics. *Earth Planet. Sci. Lett.* **487**, 221-229.

Birck J. L., Barman M. R. and Capmas F. (1997) Re-Os isotopic measurements at the femtomole level in natural samples. *Geostandards Newsletter* **21**(1)*,* 19–27.

Bouvier, A., Gattacceca, J., Agee, C., Grossman, J. and Metzler, K. (2017) The Meteoritical Bulletin, No. 105. *Meteorit. Planet. Sci*. 1, 1-250.

Brasser, R. and Mojzsis, S.J. (2020) The partitioning of the inner and outer Solar System by a structured protoplanetary disk. *Nat. Astron.* **4**, 492-499.

Breen, J.P., Rubin, A.E., and Wasson, J.T. (2016). Variations in impact effects among IIIE iron meteorites. *Meteorit. Planet. Sci.* **51**(9)*,* 1611-1631.

Buchwald V. F. (1975). Handbook of Iron Meteorites. University of California Press, 1418 pp.

Budde G., Burkhardt C., Brennecka G.A., Fischer-Godde M., Kruijer T.S. and Kleine T. (2016) Molybdenum isotopic evidence for the origin of chondrules and a distinct heritage of carbonaceous and non-carbonaceous meteorites. *Earth Planet. Sci. Lett.* **454**, 293-303.

Budde, G., Burkhardt, C. and Kleine, T. (2019) Molybdenum isotopic evidence for the late accretion of outer Solar System material to Earth. *Nat. Astron.* **3**, 736-741.

Burkhardt, C., Kleine, T., Oberli, F., Pack, A., Bourdon, B. and Wieler, R. (2011) Molybdenum isotope anomalies in meteorites: constraints on solar nebula evolution and origin of the Earth. *Earth Planet. Sci. Lett.* **312**, 390-400.

Campbell A.J. and Humayun M. (2005) Composition of group IVB irons and their parental melt. *Geochim. Cosmochim. Acta* **69**, 4733-4744.

Chabot, N. L. (2004) Sulfur contents of the parental metallic cores of magmatic iron meteorites. *Geochim*. *Cosmochim*. *Acta* **68**(17), 3607-3618.

Chabot, N. L., Wollack, E. A., McDonough, W. F., Ash, R. D. and Saslow, S. A. (2017) Experimental determination of partitioning in the Fe-Ni system for applications to modeling meteoritic metals. *Meteorit. Planet. Sci* **52**(6), 1133-1145.

Chabot, N.L. and Zhang, B. (2022) A revised trap melt model for iron meteorites applied to the IIIAB group. *Meteorit. Planet. Sci.* **57**(2), 200-227.

Chen J.H., Papanastassiou D.A. and Wasserburg G.J. (2010) Ruthenium endemic isotope effects in chondrites and differentiated meteorites. *Geochim*. *Cosmochim*. *Acta* **74**, 3851–3862.

Cohen A. S. and Waters F. G. (1996) Separation of osmium from geological materials by solvent extraction for analysis by thermal ionisation mass spectrometry. *Anal. Chim. Acta* **332**(2-3), 269–275.

Dauphas N., Davis A.M., Marty B. and Reisberg L. (2004) The cosmic molybdenum-ruthenium isotope correlation. *Earth Planet. Sci. Lett.* **226**(3-4), 465-475.

Fischer-Gödde, M., Burkhardt, C., Kruijer, T. S. and Kleine, T. (2015) Ru isotope heterogeneity in the solar protoplanetary disk. *Geochim. Cosmochim. Acta* **168**, 151–171.

Hellmann, J.L., Kruijer, T.S., Van Orman, J.A., Metzler, K. and Kleine, T. (2019) Hf-W chronology of ordinary chondrites. *Geochim. Cosmochim. Acta* **258**, 290-309.

Hilton, C.D., Bermingham, K.R., Walker, R.J. and McCoy, T.J. (2019). Genetics, crystallization sequence, and age of the South Byron Trio meteorites: New insights to carbonaceous chondrite (CC) type parent bodies. *Geochim. Cosmochim. Acta* **251**, 217-228.

Hilton C. D., Ash R. D. and Walker R. J. (2020) Crystallization histories of the group IIF iron meteorites and Eagle Station pallasites. *Meteorit. Planet. Sci*. **55**, 2570–2586.

Hilton, C.D., Ash, R.D. and Walker, R.J. (2022). Chemical characteristics of iron meteorite parent bodies. *Geochim. Cosmochim. Acta* **318**, 112-125.

Hirschmann, M.M., Bergin, E.A., Blake, G.A., Ciesla, F.J. and Li, J. (2021) Early volatile depletion on planetesimals inferred from C-S systematics of iron meteorite parent bodies. *PNAS* **118** (13).

Horan M.F., Walker R.J., Morgan J.W., Grossman J.N. and Rubin A.E. (2003). Highly siderophile elements in chondrites. *Chem. Geol.* **196**, 5-20.

Hunt, A.C., Ek, M. and Schönbächler, M. (2017) Separation of Platinum from Palladium and Iridium in iron meteorites and accurate high-precision determination of platinum isotopes by multi-collector ICP-MS. *Geostand. Geoanal. Res,* **41***,* 633-647.

Jones, J. H. and Malvin, D. J. (1990) A nonmetal interaction model for the segregation of trace metals during solidification of Fe-Ni-S, Fe-Ni-P, and Fe-Ni-SP alloys. *Metall. Trans. B* **21**, 697-706.

Kleine, T., Mezger, K., Münker, C., Palme, H. and Bischoff, A. (2004) 182Hf–182W isotope systematics of chondrites, eucrites, and Martian meteorites: chronology of core formation and mantle differentiation in Vesta and Mars. *Geochim. Cosmochim. Acta* **68**, 2935–2946.

Kleine, T. and Rudge, J.F. (2011) Chronometry of meteorites and the formation of the Earth and Moon. *Elements* **7***,* 41-46.

Kruijer, T.S., Fischer-Godde, M., Kleine, T., Sprung, P., Leya, I., and Wieler, R. (2013) Neutron capture on Pt isotopes in iron meteorites and the Hf-W chronology of core formation in planetesimals. *Earth Planet. Sci. Lett.* **361**, 162-172.

Kruijer, T.S., Kleine, T., Fischer-Gödde, M., Burkhardt, C. and Wieler, R. (2014) Nucleosynthetic W isotope anomalies and the Hf-W chronometry of Ca-Al-rich inclusions. *Earth Planet. Sci. Lett.* **403**, 317-327.

Kruijer, T. S., Burkhardt, C., Budde, G., and Kleine, T. (2017). Age of Jupiter inferred from the distinct genetics and formation times of meteorites. *PNAS* 201704461.

Lichtenberg, T., Drążkowska, J., Schönbächler, M., Golabek, G.J. and Hands, T.O. (2021) Bifurcation of planetary building blocks during Solar System formation. *Science* **371**, 365-370.

Lodders K., Fegley B. (1998) *The planetary scientist's companion*. Oxford University Press, New York, p. 371.

Lodders, K. (2003) Solar System abundances and condensation temperatures of the elements. *Astrophys. J.* **591**, 1220-1247.

Lu, Q. and Masuda, A. (1994) The isotopic composition and atomic weight of molybdenum. *Int. J. Mass Spectrom. Ion Processes*. **130**(1-2), 65–72.

Ludwig, K. R. (2003). User's manual for Isoplot 3.00. *Berkeley Geochronology Center Special Publication* No. 4, Berkeley, CA, 70 pp.

Malvin, D.J., Wang, D. and Wasson, J.T. (1984) Chemical classification of iron meteorites -X. Multielement studies of 43 irons, resolution of group IIIE from IIIAB, and evaluation of Cu as a taxonomic parameter. *Geochim. Cosmochim. Acta* **48**, 785-804.

Markowski, A., Leya, I., Quitte, G., Ammon, K., Halliday, A.N. and Wieler, R. (2006) Correlated helium-3 and tungsten isotopes in iron meteorites: Quantitative cosmogenic corrections and planetesimal formation times. *Earth Planet. Sci. Lett.* **250***,* 104-115.

McCoy, T.J., Walker, R.J., Goldstein, J.I., Yang, J., McDonough, W.F., Rumble, D., Chabot, N.L., Ash, R.D., Corrigan, C.M., Michael, J.R. and Kotula, P.G. (2011) Group IVA irons: New constraints on the crystallization and cooling history of an asteroidal core with a complex history. *Geochim. Cosmochim. Acta* **75**, 6821-6843.

720 Moore, C.B., Lewis, C.F. and Nava, D. (1969) Superior Analyses of Iron Meteorites.
721 *Meteorite Research, 738-748.*
722
723 Nagai, Y. and Yokoyama, T. (2014) Chemical separation of Mo and W from terrestrial and
724 extraterrestrial samples via anion exchange chromatography. *Anal. Chem.* **86**(10),
725 4856-4863.
726
727 Pernicka, E. and Wasson, J.T. (1987) Ru, Re, Os, Pt and Au in iron meteorites. *Geochim.*
728 *Cosmochim. Acta* **51**, 1717-1726.
729
730 Poole, G. M., Rehkamper, M., Coles, B. J., Goldberg, T. and Smith, C. L. (2017)
731 Nucleosynthetic molybdenum isotope anomalies in iron meteorites–new evidence
732 for thermal processing of solar nebula material. *Earth Planet. Sci. Lett.* **473**, 215-
733 226.
734
735 Rehkämper, M. and Halliday, A. N. (1997) Development and application of new ion-
736 exchange techniques for the separation of the platinum group and other siderophile
737 elements from geological samples. *Talanta* **44**(4), 663-672.
738
739 Rusk B. (2009) Laser ablation ICP-MS in the earth sciences: Current practices and
740 outstanding issues. *Econ. Geol.* **104**(4), 601–602.
741
742 Scott, E. R., Wasson, J. T. and Buchwald V.F. (1973) The chemical classification of iron
743 meteorites - VII. A reinvestigation of irons with Ge concentrations between 25 and
744 80 ppm. *Geochim. Cosmochim. Acta* **37***,*1957-1983.
745
746 Spitzer, F., Burkhardt, C., Budde, G., Kruijer, T.S., Morbidelli, A. and Kleine, T. (2020)
747 Isotopic evolution of the inner solar system inferred from molybdenum isotopes in
748 meteorites. Astrophys. J. **898**, 10pp.
749

Spitzer, F., Burkhardt, C., Nimmo, F., Kleine, T. (2021) Nucleosynthetic Pt isotope anomalies and the Hf-W chronology of core formation in inner and outer solar system planetesimals. *Earth Planet. Sci. Lett.* **576**, 117211.

Sugiura, N., Ikeda, Y., Zashu, S. and Wasson, J.T. (2000) Nitrogen-isotopic compositions of IIIE iron meteorites. *Meteorit. Planet. Sci*. **35**, 749-756.

Tornabene, H.A., Hilton, C.D., Bermingham, K.R., Ash, R.D. and Walker, R.J. (2020) Genetics, age, and crystallization history of group IIC iron meteorites. *Geochim. Cosmochim. Acta* **288***,* 36-50.

Trinquier, A., Birck, J.-L. and Allégre, C.J. (2007) Widespread 54Cr heterogeneity in the inner solar system. *Astropys. J.* **655**(2), 1179-1185.

Trinquier, A., Elliot, T., Ulfbeck, D., Coath, C., Krot, A.N. and Bizzarro, M. (2009) Origin of nucleosynthetic isotope heterogeneity in the solar protoplanetary disk. *Science* **324**(5925), 374-376.

Vockenhuber, C., Oberli, F., Bichler, M., Ahmad, I., Quittem, G., Meier, M., Halliday, A.N., Lee, D.-C., Kutschera, W., Steier, P., Gehrke, R.J. and Helmer R.G. (2004) New half-life measurement of 182Hf: Improved chronometer for the early solar system. *Phys. Rev. Lett.* **93**(17), 172501.

Völkening, J., Köppe, M. and Heumann, K.G. (1991) Tungsten isotope ratio determinations by negative thermal ionization mass spectrometry. *Int. J. Mass Spectrom*. *Ion Processes.* **107**(2), 361–368.

Walker, R. J., McDonough, W. F., Honesto, J., Chabot, N. L., McCoy, T. J., Ash, R. D. and Bellucci, J. J. (2008) Modeling fractional crystallization of group IVB iron meteorites. *Geochim. Cosmochim. Acta* **72**(8), 2198-2216.

781 Warren, P. H. (2011) Stable-isotopic anomalies and the accretionary assemblage of the
782 Earth and Mars: A subordinate role for carbonaceous chondrites. *Earth Planet. Sci.*
783 *Lett.* **311**(1-2), 93-100.
784
785 Wasson, J.T. (1999). Trapped melt in IIIAB irons: Solid/liquid elemental partitioning
786 during the fractionation of the IIIAB magma. *Geochim. Cosmochim. Acta* **63**(8),
787 2875– 2889.
788
789 Wasson, J.T. and Richardson, J.W. (2001) Fractionation trends among IVA iron
790 meteorites: Contrasts with IIIAB trends. *Geochim. Cosmochim. Acta* **65**(6), 951–
791 970.
792
793 Wittig, N., Humayun, M., Brandon, A.D., Huang, S. and Leya I. (2013) Coupled W-Os-Pt
794 isotope systematics in IVB iron meteorites: In situ neutron dosimetry for W isotope
795 chronology. *Earth Planet. Sci. Lett.* **361**, 152-161.
796
797 Worsham, E.A., Walker, R.J. and Bermingham, K.R. (2016a) High-precision molybdenum
798 isotope analysis by negative thermal ionization mass spectrometry. *Int. J. Mass*
799 *Spectrom.* **407**, 51-61.
800
801 Worsham, E.A., Bermingham, K.R. and Walker, R.J. (2016b) Siderophile element
802 systematics of IAB complex iron meteorites: new insights into the formation of an
803 enigmatic group. *Geochim. Cosmochim*. *Acta* **188**, 261-283.
804
805 Worsham, E.A., Burkhardt, C., Budde, G., Fischer-Gödde, M., Kruijer, T.S. and Kleine, T.
806 (2019) Distinct evolution of the carbonaceous and non-carbonaceous reservoirs:
807 insights from Ru. Mo, and W isotopes. *Earth Planet. Sci. Lett.* **521**, 103-112.
808
809 Zhang, B., Chabot, N.L., Rubin, A.E., Humayun, M., Boesenberg, J.S. and van Niekerk,
810 D. (2022) Chemical study of group IIIF iron meteorites and the potentially related

811 pallasites Zinder and Northwest Africa 1911. *Geochim. Cosmochim. Acta* **323***,* 202-
812 219.
813
814 Zhang, B., Chabot, N.L., Rubin, A.E. (2022) Compositions of carbonaceous-type
815 asteroidal cores in the early solar system. *Sci. Adv.* 8, eabo5781.

Table 1. Average siderophile element concentrations for the group IIIE irons determined by LA-ICP-MS.

	Aletai *(an.)*	Coopertown	Kokstad	Burlington	Tanokami Mountain	Staunton	Paloduro	Colonia Obrera	Rhine Villa	Willow Creek
Re	0.05	b.d.	0.05	b.d.	b.d.	b.d.	b.d.	0.005	b.d.	b.d.
Os	0.26 ± 0.02	0.18 ± 0.02	0.16 ± 0.01	0.15 ± 0.04	0.06 ± 0.01	0.05 ± 0.03	0.05 ± 0.01	0.05 ± 0.02	0.04 ± 0.01	0.01 ± 0.01
W	0.5 ± 0.2	0.95 ± 0.13	0.89 ± 0.08	0.9 ± 0.3	1.1 ± 0.5	0.76 ± 0.23	1.1 ± 0.8	0.92 ± 0.9	0.66 ± 0.1	0.62 ± 0.03
Ir	0.26 ± 0.06	0.60 ± 0.06	0.56 ± 0.03	0.51 ± 0.03	0.21 ± 0.06	0.12 ± 0.04	0.17 ± 0.18	0.09 ± 0.04	0.11 ± 0.03	0.05 ± 0.03
Mo	7.1 ± 4.1	7.2 ± 0.1	6.2 ± 0.8	7.0 ± 0.4	9.6 ± 4.5	7.6 ± 1.1	7.4 ± 1.6	7.6 ± 1.4	6.0 ± 0.2	7.2 ± 0.2
Ru	1.5 ± 0.5	5.7 ± 1.5	5.7 ± 1.1	5.3 ± 1.2	6.0 ± 2.1	4.0 ± 0.3	4.0 ± 2.4	3.1 ± 0.7	3.6 ± 0.4	3.1 ± 1.0
Pt	2.5 ± 0.4	8.9 ± 0.4	8.9 ± 0.9	8.9 ± 0.3	7.9 ± 2.8	6.2 ± 0.4	6.0 ± 0.8	5.5 ± 0.5	5.8 ± 0.3	5.0 ± 0.5
Rh	0.9 ± 0.1	1.3 ± 0.2	1.2 ± 0.1	1.2 ± 0.1	1.7 ± 0.7	1.2 ± 0.1	1.2 ± 0.4	1.3 ± 0.1	1.2 ± 0.1	1.1 ± 0.2
Ni	8.8 ± 5.1	7.9 ± 1.8	7.8 ± 0.8	7.7 ± 0.6	13.3 ± 0.6	8.3 ± 0.8	9.4 ± .6	10.2 ± 2.4	7.4 ± 1.3	8.2 ± 3.0
Co	0.57 ± 0.08	0.52 ± 0.04	0.50 ± 0.01	0.51 ± 0.01	0.52 ± 0.12	0.51 ± 0.03	0.49 ± 0.11	0.50 ± 0.04	0.52 ± 0.03	0.52 ± 0.08
Fe	90.6 ± 5.1	91.5 ± 1.7	91.6 ± 0.8	91.7 ± 0.6	86.1 ± 0.7	91.1 ± 0.7	90.0 ± 0.6	89.2 ± 2.4	92.0 ± 1.3	91.2 ± 0.2
Pd	5.5 ± 3.2	2.3 ± 0.8	2.4 ± 0.4	2.3 ± 0.2	3.7 ± 0.02	2.7 ± 0.2	3.2 ± 2.1	4.3 ± 0.5	2.5 ± 0.3	2.9 ± 0.24
Cr	36.7 ± 28.9	170 ± 189	64.9 ± 20.4	14.3 ± 3.1	27.0 ± 16.3	25.1 ± 16.8	25.7 ± 6.8	16.2 ± 5.9	15.4 ± 5.5	30.8 ± 43.5
P	0.16 ± 0.06	0.18 ± 0.07	0.16 ± 0.07	0.15 ± 0.04	0.16 ± 0.02	0.22 ± 0.07	0.30 ± 0.07	0.22 ± 0.07	0.12 ± 0.08	0.28 ± 0.03
As	19.4 ± 4.2	5.2 ± 1.9	4.9 ± 0.2	6.6 ± 0.6	7.6 ± 1.3	7.0 ± 1.2	6.3 ± 2.7	10.5 ± 3.2	6.5 ± 0.8	8.9 ± 0.1
Au	1.7 ± 0.7	0.46 ± 0.12	0.49 ± 0.12	0.79 ± 0.1	0.94 ± 0.1	0.73 ± 0.1	1.0 ± 0.6	1.0 ± 0.1	0.66 ± 0.1	0.98 ± 0.3
Ga	18 ± 1	17 ± 1	18 ± 1	18 ± 2	26 ± 3	19 ± 2	20 ± 1	23 ± 5	18 ± 1	19 ± 2
Ge	33 ± 3	36 ± 4	35 ± 1	37 ± 2	49 ± 12	40 ± 6	37 ± 5	42 ± 2	39 ± 1	40 ± 1
n	4	3	3	2	2	3	3	3	3	2

Iron, Ni, Co, and P concentrations reported in wt. %, all other elements reported in ppm. 2σ values of repeated measurement along ablation tracks are reported as uncertainties. *n* is number of lines measured for each sample. Samples are in order of decreasing Os concentration.

b.d. below detection limits.

821 **Table 2.** Rhenium-Os isotopic and HSE composition data, obtained by isotope dilution for ten IIIE irons.

Sample	Wt.	Re	Os	Ir	Ru	Pt	Pd	$^{187}Re/^{188}Os$	2σ	$^{187}Os/^{188}Os$	2σ
Aletai *(an.)*	0.1491	19.57	201.9	230.4	1432	2001	5491	0.4671	0.0005	0.13211	0.00013
Coopertown	0.0946	40.24	189.8	599.4	6697	9603	3379	1.028	0.0010	0.17662	0.00018
Kokstad	0.0770	38.86	203.1	567.4	6306	9386	3407	0.9004	0.0009	0.16711	0.00017
Burlington	0.0999	31.89	153.8	485.2	5555	8673	3033	1.005	0.0010	0.17512	0.00013
Tanokami Mountain	0.1366	10.91	65.88	123.9	4080	6786	3107	0.8008	0.0008	0.15824	0.00016
Staunton	0.1636	12.73	72.17	129.4	4705	6894	3586	0.8544	0.0009	0.16377	0.00016
Paloduro	0.2009	8.267	47.66	119.7	4389	6744	3672	0.8396	0.0008	0.16115	0.00016
Colonia Obrera	0.1664	4.072	23.89	64.18	3165	4837	3798	0.7542	0.0008	0.15678	0.00016
Rhine Villa	0.2253	7.608	42.62	110.3	4121	6326	3406	0.8641	0.0009	0.16469	0.00016
Willow Creek	0.1196	4.095	22.86	53.08	3273	5192	3518	0.8339	0.0008	0.16292	0.00016

822 Sample weights reported in grams. Elemental concentrations reported in ppb.

Table 3. Platinum isotopic compositions of select IIIE irons.

Sample	*n*	$\mu^{196}Pt$	±
Aletai *(an.)*	3	27	8
Coopertown	3	3	8
Kokstad	3	22	8
Burlington	3	10	8
Tanokami Mountain	2	26	8

n is number of analyses. Uncertainties reflect the 2SD of the standards run during the analytical campaign.

826 **Table 4.** Measured Mo and Ru isotopic compositions for select IIIE irons. Group IIIE
827 average is corrected for CRE.

	n	μ^{92}Mo	±	μ^{94}Mo	±	μ^{95}Mo	±	μ^{97}Mo	±	μ^{100}Mo	±	*n*	μ^{100}Ru	±
Coopertown	2	106	41	100	14	51	8	21	6	20	22	3	-42	8
Kokstad	2	96	37	92	12	37	8	19	5	13	20	3	-34	8
Burlington	2	119	37	97	12	41	8	22	5	17	20	3	-45	8
Tanokami Mountain	1	70	42	80	13	27	10	25	4	22	22	2	-28	8
IIIE Average[a]	7	124	40	104	14	52	10	19	5	18	20	11	-47	9
Aletai *(an.)*	3	129	41	113	14	48	8	22	6	29	22	2	-42	8

828 *n* is number of analyses. Uncertainties reflect the 2SD of the standards run during the
829 analytical campaign for that sample.
830 [a] Group average was calculated using slopes obtained from μ^{i}Mo vs. μ^{196}Pt regressions
831 calculated via *ISOPLOT*.

Table 5. Tungsten isotopic compositions for select IIIE irons.

	n	$\mu^{182}W_{Measured\ (6/4)}$	±	$\mu^{183}W_{Measured}$	±	$\mu^{182}W_{Corrected}$	±	ΔT_{CAI}	±
Coopertown	1	-338	6	2	3	-335	10	1.2	0.9
Kokstad	1	-352	6	0	3	-331	10	1.6	0.9
Burlington	2	-335	7	-2	3	-326	10	2.1	1.0
IIIE Average[a]	4	-342	6	0	3	-331	10	1.6	0.9
Aletai *(an.)*[b]	1	-361	6	-1	3	-335	10	1.2	0.9

n is number of analyses. Uncertainties reflect the 2SD of the standards run during the analytical campaign. [a] Group average was calculated using slopes obtained from $\mu^{182}W$ vs. $\mu^{196}Pt$ regression calculated via *ISOPLOT*. [b] The $\mu^{182}W$ value for Aletai was corrected using the slope obtained from the $\mu^{182}W$ vs. $\mu^{196}Pt$ regression for the IIIE irons.

837 **Table 6.** Calculated HSE concentrations for the model discussed in the text, and proposed
838 parental melt compositions for the IIIAB, IIAB, IVA, IVB, IIC, and South Byron Trio
839 (SBT) systems for comparison.

	Re	Os	Ir	Ru	Pt	Pd
NC-type						
IIIE	220	2700	2500	3600	5600	3600
IIAB[a]	260	2900	2900	4800	6500	2100
IC[b]	150	1700	1700	2400	3200	2100
IIIAB[a]	260	2800	2800	4400	5900	3100
IVA[c]	295	3250	2700	3900	5900	4500
CC-type						
IIC[d]	280	3350	3050	4340	6070	5300
IID[a]	370	4400	4100	6300	8000	4300
IIF[e]	355	4200	4200	6800	8200	4250
IIIF[a]	275	3600	3100	4300	6100	4000
IVB[f]	1410	21600	17500	19600	29800	10900
SBT[g]	770	9400	8500	13000	16000	84000

840 all concentrations are in ppb. Data from [a]Hilton et al. (2022), [b]Tornabene et al. (2022),
841 [c]McCoy et al. (2011), [d]Tornabene et al. (2020), [e]Hilton et al. (2020), [f]Walker et al. (2008),
842 and [g]Hilton et al. (2019).

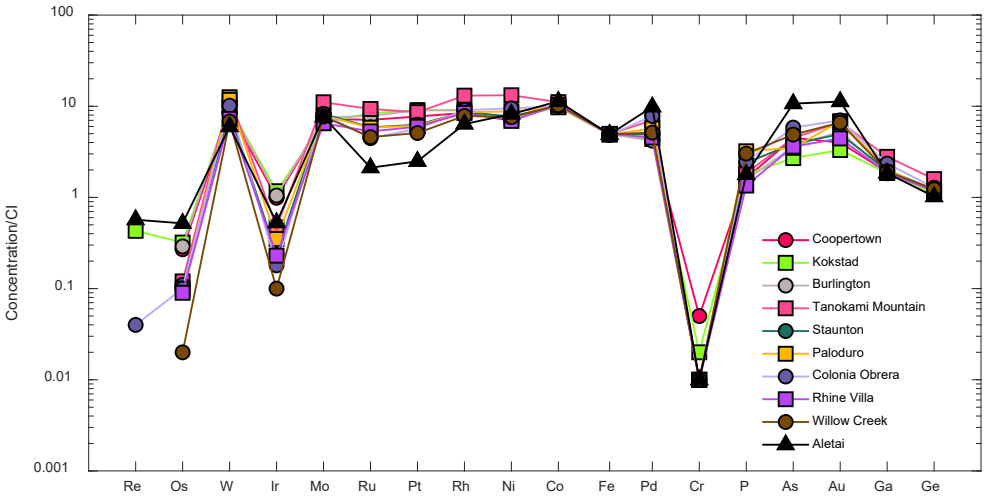

843

844 **Figure 1.** CI-chondrite normalized siderophile element abundances for nine group IIIE iron
845 meteorites and Aletai obtained via laser ablation ICP-MS. Normalizing data are from
846 Lodders (2003). Elements are listed in order of decreasing 50% condensation temperature
847 from left to right (Lodders, 2003).

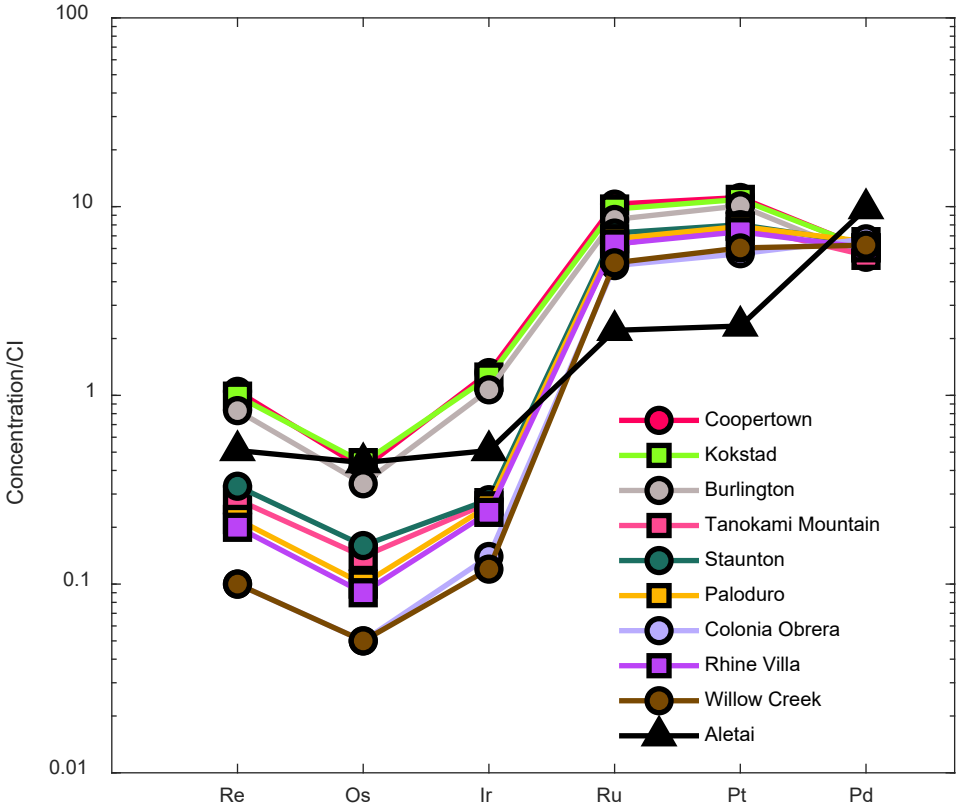

Figure 2. Bulk CI chondrite normalized HSE abundance plot of nine IIIE irons and the anomalous IIIE iron Aletai obtained via isotope dilution. Bulk composition data were normalized to concentrations obtained by isotope dilution for the CI chondrite Orgueil (Horan et al., 2003). Note the pattern obtained for Aletai differs from that of the other IIIE irons. Uncertainties are smaller than symbol sizes.

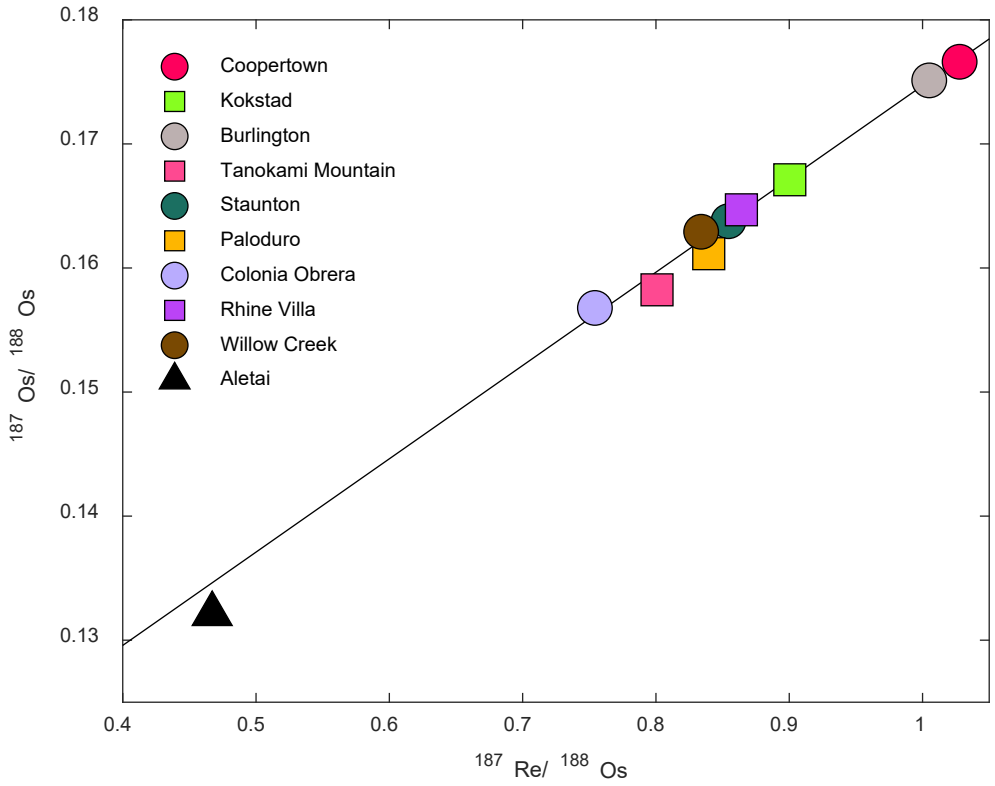

Figure 3. $^{187}Re/^{188}Os$ vs. $^{187}Os/^{188}Os$ isochron plot for the group IIIE iron meteorites. Data are shown relative to a 4.56 Ga chondritic reference isochron. Uncertainties are smaller than the symbol size.

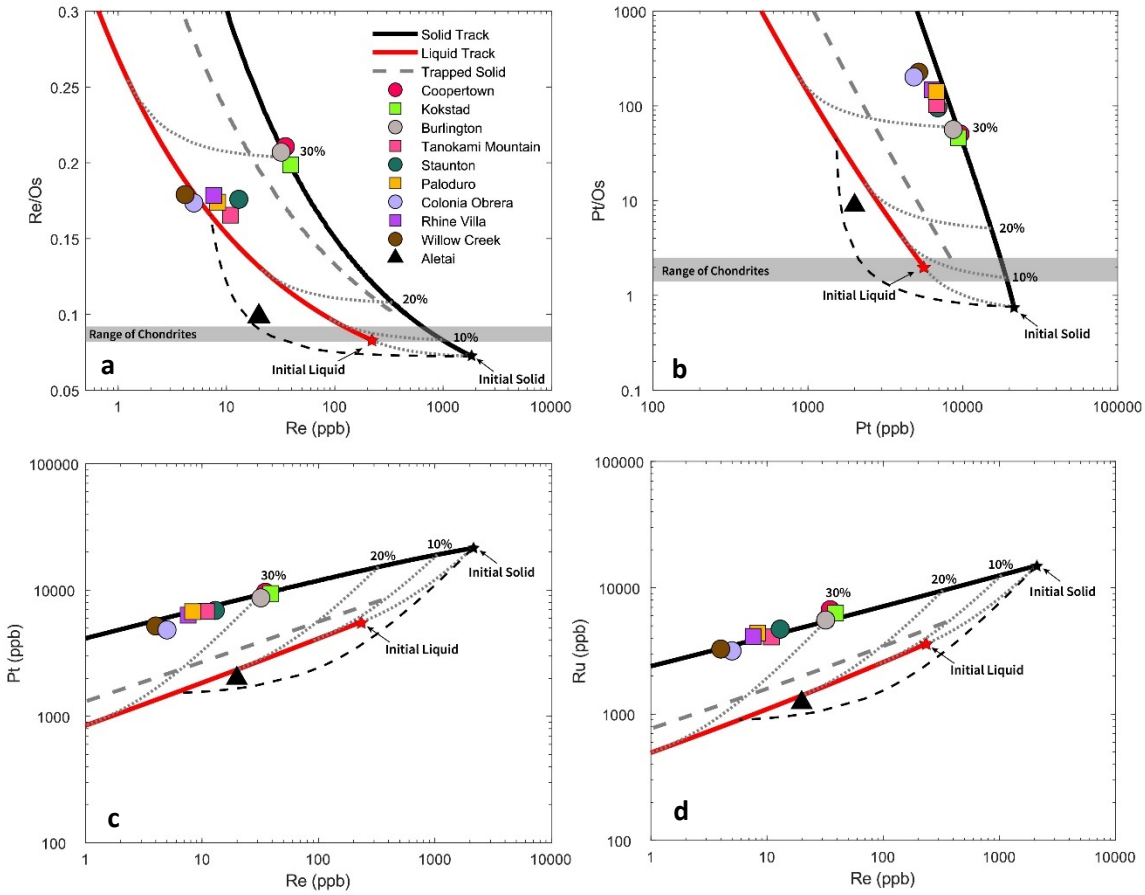

858 **Figure 4.** Best-fit fractional crystallization model for Re (ppb) vs. Re/Os (a), Pt (ppb) vs.
859 Pt/Os (b), Re (ppb) vs. Pt (ppb) (c), and Re (ppb) vs. Ru (ppb) (d) systematics for the IIIE
860 iron meteorites. Small dotted gray lines represent solid metal-liquid metal mixing curves
861 for the labeled increments of fractional crystallization. Black dashed lines represent
862 mixing between an evolved liquid composition and early formed solid.

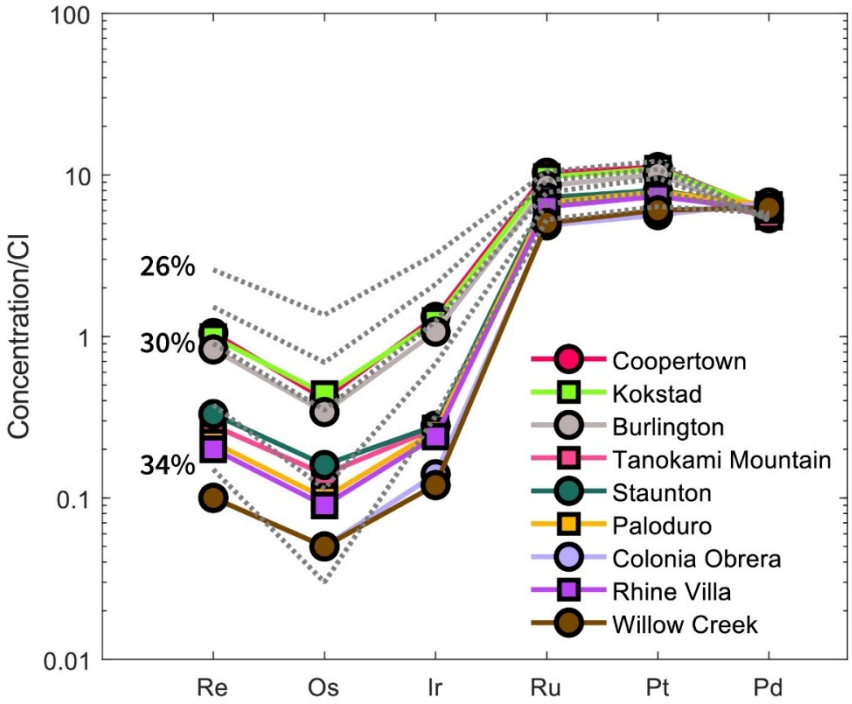

Figure 5. Modeled bulk CI chondrite normalized equilibrium solid compositions at 2 wt.% increments under the conditions of the proposed fractional crystallization model. The measured HSE concentrations of the IIIE irons are shown for comparison. Aletai is not included. Isotope dilution data for the CI chondrite Orgueil are used for normalization (Horan et al., 2003).

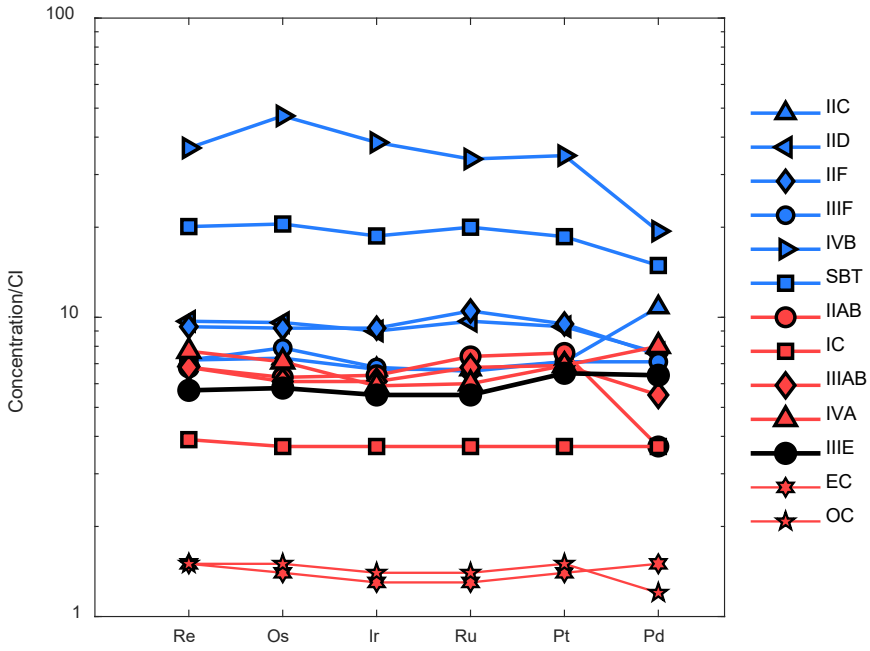

868 **Figure 6.** CI chondrite normalized calculated HSE parent melt composition of the IIIE
869 iron meteorites with parent melts of other iron meteorite groups for comparison. Data for
870 other groups is from Table 6. CI chondrite data is from Horan et al. (2003) for Orgueil.
871 Average compositions for ordinary (OC) and enstatite (EC) chondrites are included as well
872 (Horan et al., 2003). Red lines and symbols correspond to NC-type iron meteorites, and
873 blue lines and symbols correspond to CC-type iron meteorites.

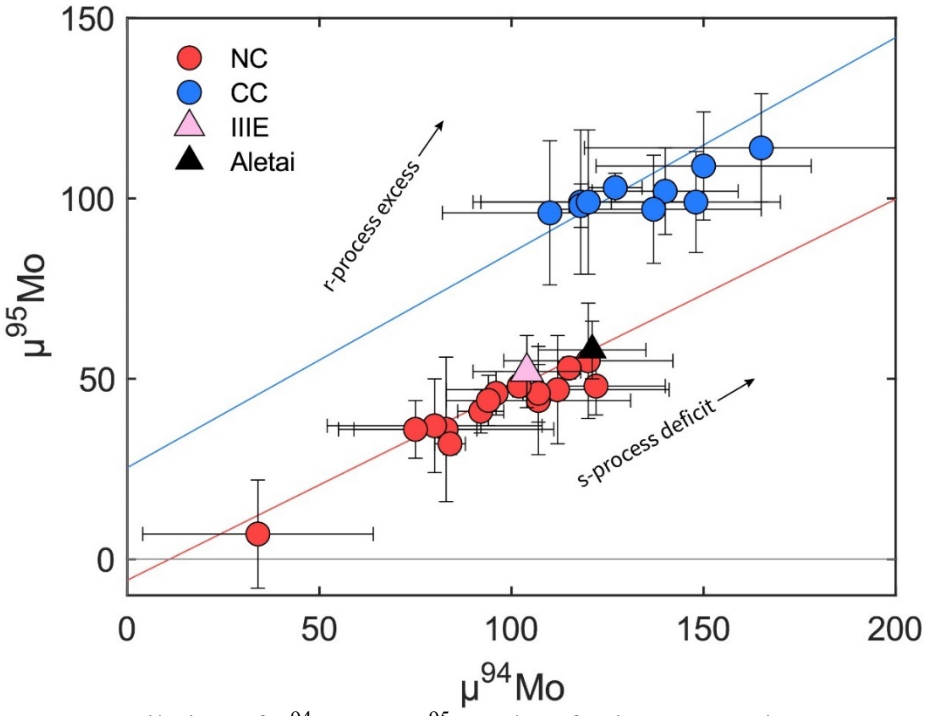

Figure 7. Compilation of μ^{94}Mo vs. μ^{95}Mo data for iron meteorites. Data compiled from Poole et al. (2017), Bermingham et al. (2018), Worsham et al. (2019), Hilton et al. (2019), and Tornabene et al. (2020). Blue symbols represent CC-type iron meteorites (IID, IIF, IIIF, IVB, South Byron Trio, and the ungrouped iron meteorites Dronino, Tishomingo, and Chinga). Red symbols represent NC-type iron meteorites (IC, IIAB, IIIAB, IVA, and the ungrouped iron meteorite Gebel Kamil). Red and blue lines represent NC and CC lines reported by Spitzer et al. (2020) and Budde et al. (2019), respectively. Data from this study for the IIIE irons and Aletai are also plotted, represented by the pink and black triangles, respectively.

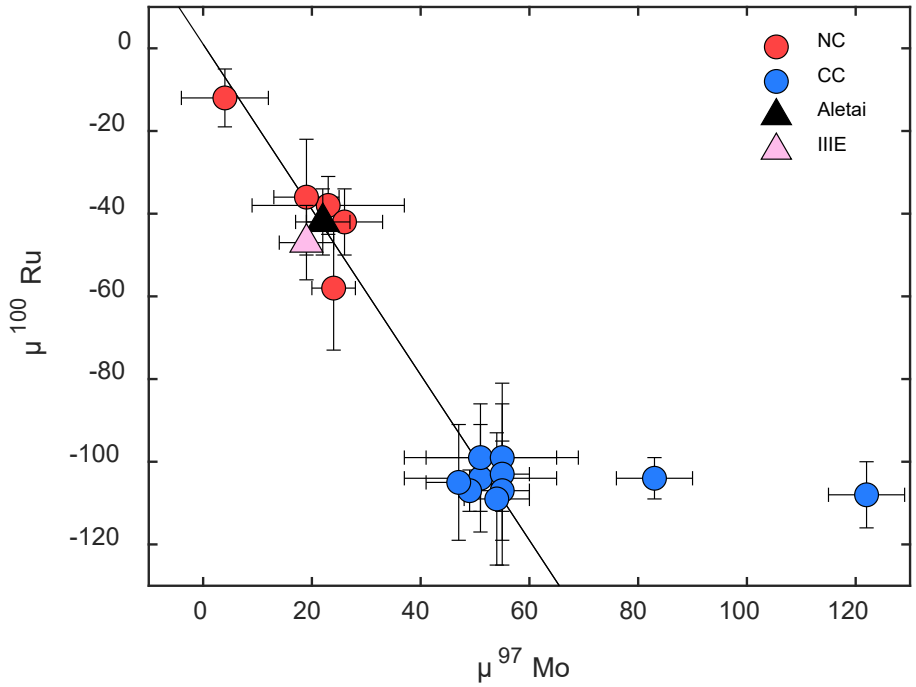

Figure 8. Plot of μ^{97}Mo and μ^{100}Ru for iron meteorites. Data compiled from Worsham et al. (2019), Bermingham et al. (2018), and Hilton et al. (2019). Blue symbols represent CC-type iron meteorites (IID, IIF, IIIF, IVB, South Byron Trio, and the ungrouped iron meteorites Dronino, Tishomingo, and Chinga). Red symbols represent NC-type iron meteorites (IC, IIAB, IIIAB, IVA, and the ungrouped iron meteorite Gebel Kamil). The black line represents the regression of the Mo-Ru correlation from Bermingham et al. (2018). Data from this study for the IIIE irons and Aletai are also plotted, represented by the pink and black triangles, respectively.

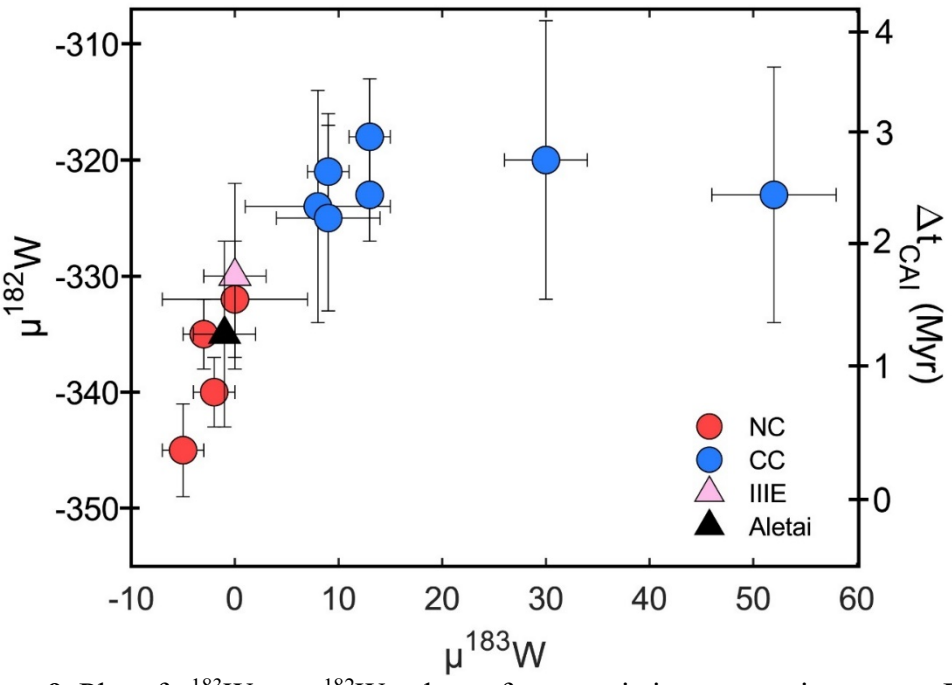

Figure 9. Plot of $\mu^{183}W$ vs. $\mu^{182}W$ values of magmatic iron meteorite groups. Right y-axis represents time of metal-silicate segregation, relative to CAI formation, in Myr. Data compiled from Kruijer et al. (2017) and Hilton et al. (2019). All ages were calculated using a carbonaceous chondrite $\mu^{182}W$ value. Blue symbols represent CC-type iron meteorites (IIC, IID, IIF, IIIF, IVB, South Byron Trio, and Wiley). Red symbols represent NC-type iron meteorites (IC, IIAB, IIIAB, and IVA). Data from this study for the IIIE irons and Aletai are also plotted, represented by the pink and black triangles, respectively.

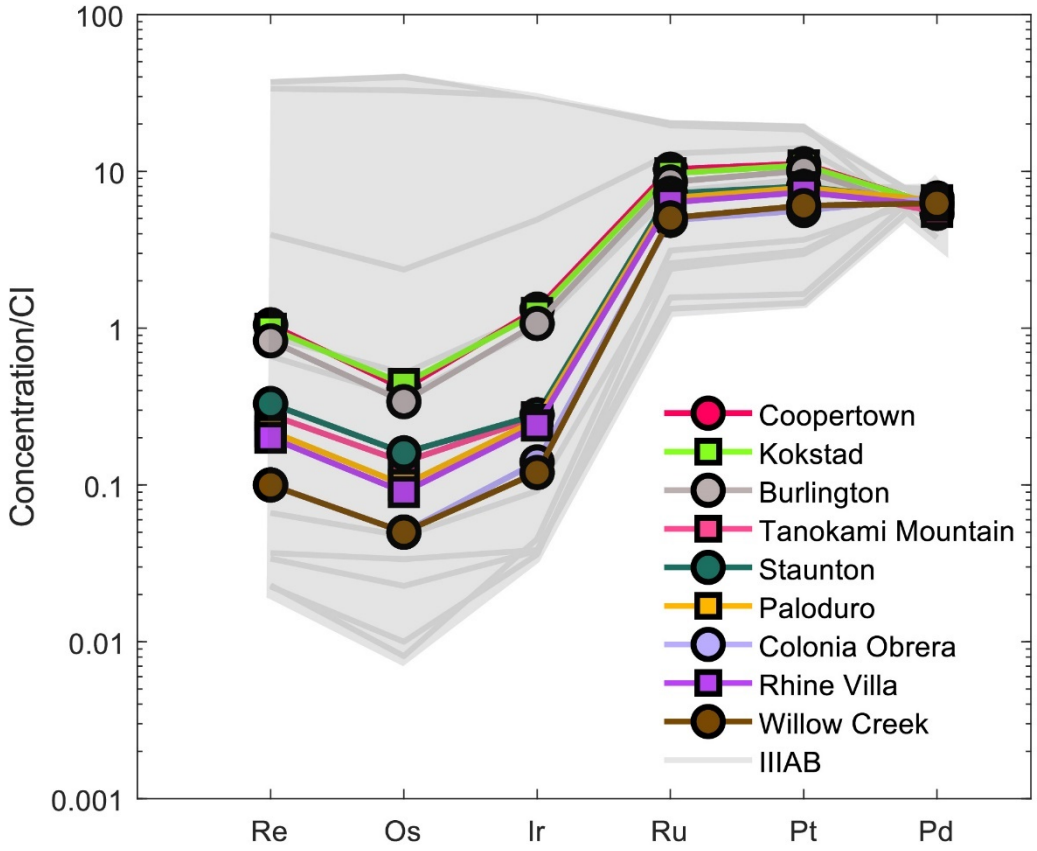

899 **Figure 10.** Bulk CI chondrite normalized HSE abundance plot of nine IIIE irons obtained
900 in this study via isotope dilution. Highly siderophile element abundances for the IIIAB
901 irons are represented by the gray lines and light gray field. Data for the IIIAB irons are
902 from Hilton et al. (2022) and Table S4. Bulk composition data were normalized to
903 concentrations obtained by isotope dilution for the CI chondrite Orgueil (Horan et al.,
904 2003).